Resolving Long-Standing E-Region Data/Model Discrepancies

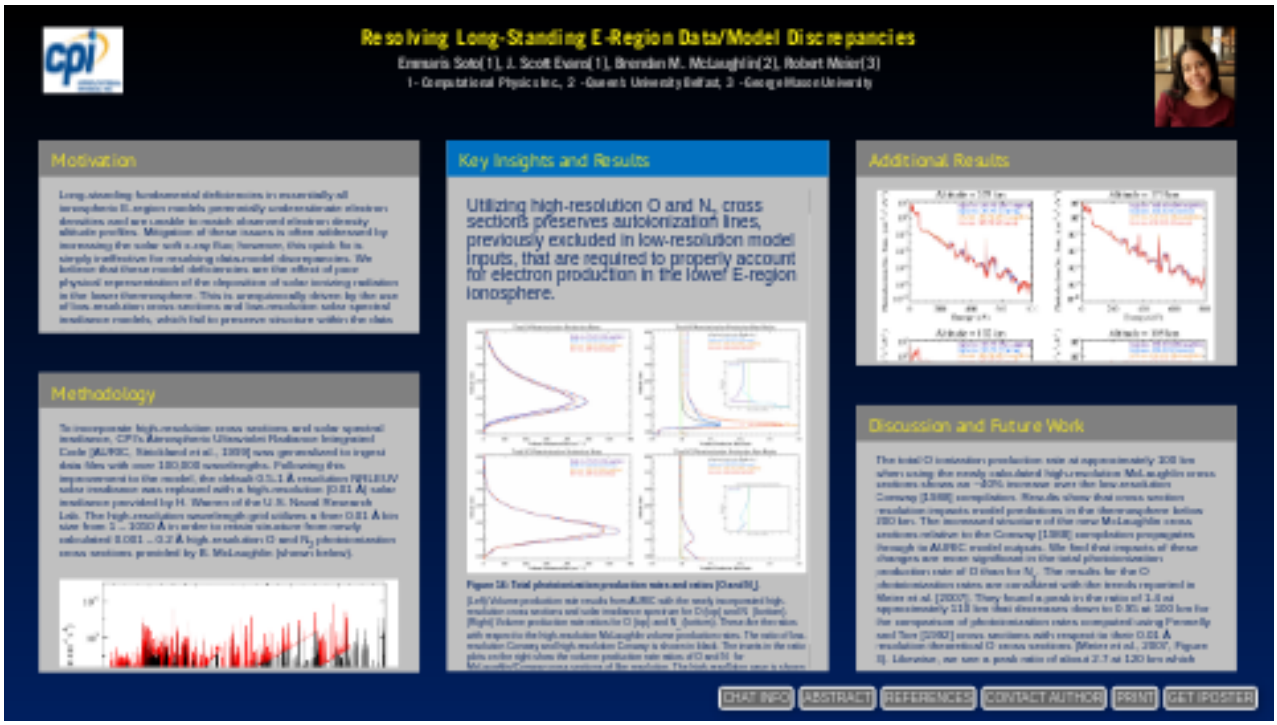

Emmaris Soto[1], J. Scott Evans[1], Brendan M. McLaughlin[2], Robert Meier[3]

1- Computational Physics Inc., 2 - Queen's University Belfast, 3 - George Mason University

PRESENTED AT:

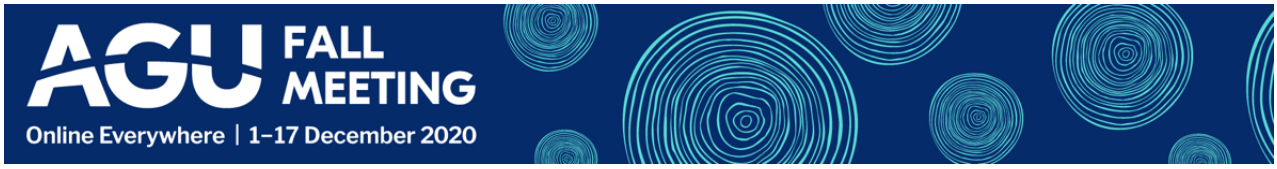

MOTIVATION

Long-standing fundamental deficiencies in essentially all ionospheric E-region models perennially underestimate electron densities and are unable to match observed electron density altitude profiles. Mitigation of these issues is often addressed by increasing the solar soft x-ray flux; however, this quick fix is simply ineffective for resolving data-model discrepancies. We believe that these model deficiencies are the effect of poor physical representation of the deposition of solar ionizing radiation in the lower thermosphere. This is unequivocally driven by the use of low-resolution cross sections and low-resolution solar spectral irradiance models, which fail to preserve structure within the data that directly impacts radiative processes in the E-region. To resolve data-model discrepancies, we utilize new high-resolution (0.01 Å) atomic oxygen and molecular nitrogen photoionization cross sections and solar spectral irradiances in order to account for the increase in the photoelectron flux at lower altitudes caused by the penetration of high-resolution photoionizing solar radiation.

METHODOLOGY

To incorporate high-resolution cross sections and solar spectral irradiance, CPI's Atmospheric Ultraviolet Radiance Integrated Code [AURIC, Strickland et al., 1999] was generalized to ingest data files with over 100,000 wavelengths. Following this improvement to the model, the default 0.5-1 Å resolution NRLEUV solar irradiance was replaced with a high-resolution (0.01 Å) solar irradiance provided by H. Warren of the U.S. Naval Research Lab. The high-resolution wavelength grid utilizes a finer 0.01 Å bin size from 1 – 1050 Å in order to retain structure from newly calculated 0.001 – 0.2 Å high-resolution O and N_2 photoionization cross sections provided by B. McLaughlin (shown below).

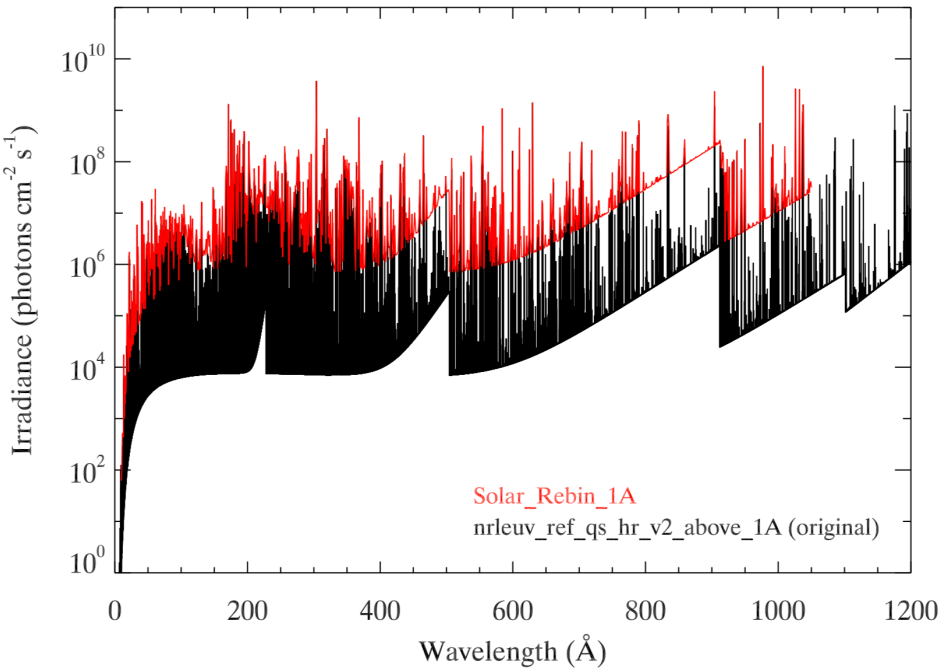

Figure 1: Comparison of high-resolution (0.01 Å) NRLEUV solar irradiance provided by H. Warren (black) and the same spectrum re-binned onto the low-resolution grid (red) with bin size of 0.5 Å below 100 Å and 1 Å from 100 to 1050 Å.

The default photoionization cross sections used with AURIC are the Conway [1988] compilation, which provide six O states and ten N_2 states. Through the application of the state-of-the-art R-matrix with pseudo-states method (RMPS) [Tayal et al., 2016; McLaughlin et al., 2011, 2013; Abdel-Nady et al., 2013; Scully et al., 2006] all transitions within the n=2 and n=3 manifolds of O are derived for the newly constructed cross section (Figures 2 – 6). The O photoionization cross sections contain 34 levels, including a k-shell calculation with 910 levels. The Conway compilation provides only six atomic oxygen ionization states; therefore, a pseudo cross section state, which accounts for the remaining 29 ion states provided by McLaughlin, was produced and incorporated into AURIC model calculations for completeness. The high- and low-resolution pseudo states exhibit a "hump" at short wavelengths that results from smoothly fitting over the

gap in the high-resolution absolute total (ABS) data (Figure 8) from 57 Å down to 41 Å. In future analyses, we will include all 34 individual states. The new N_2 cross sections provide three high-resolution states, which represent the dominant states. The AURIC comparisons presented here represent model outputs using the Conway [1988] tabulation of cross sections as well as B. McLaughlin's newly-computed high-resolution atomic oxygen and molecular nitrogen photoionization cross sections. The O_2 cross sections used are from the default Conway [1988] compilation. Model calculations using these two sets of cross sections are labeled as Conway and McLaughlin, respectively, in the figures.

Comparison of high-resolution cross sections to Conway [1988] compilation shown on three different grids: original (left), high-resolution (middle), and low-resolution (right).

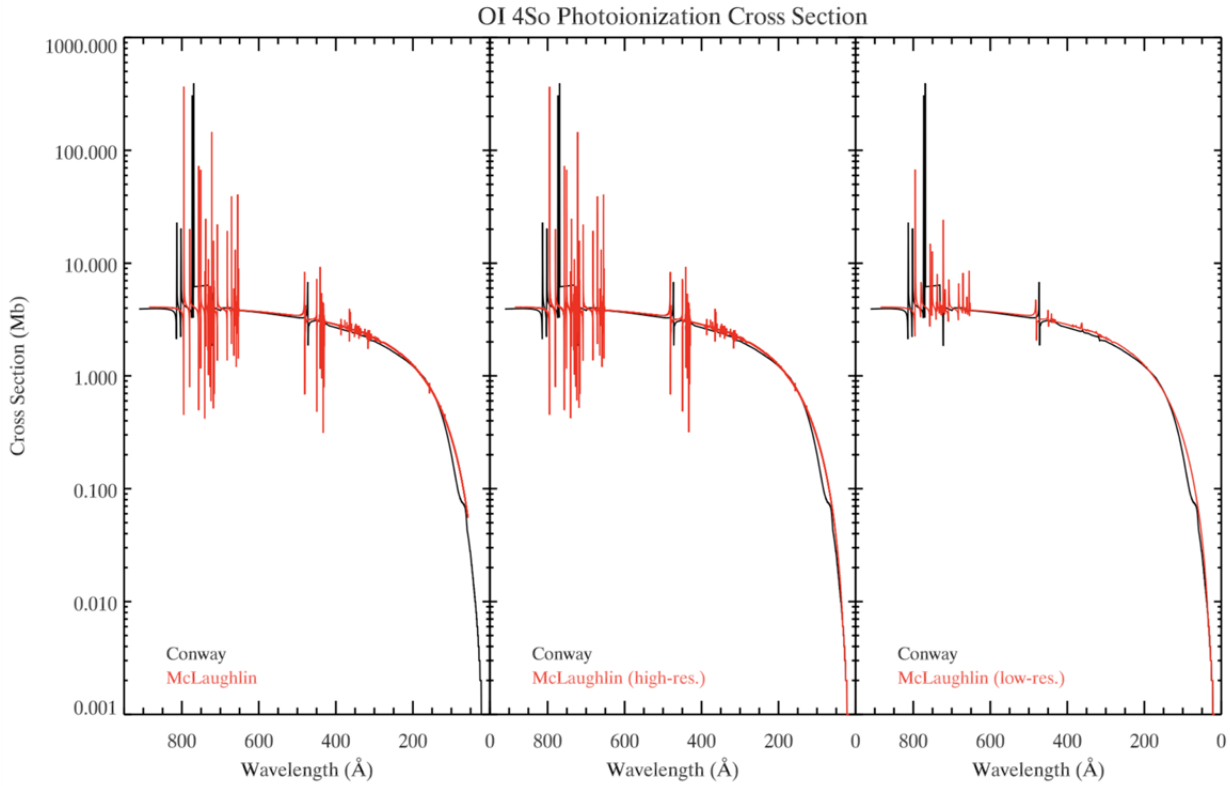

Figure 2: $O^+2s2p^3\ ^4S_0$ Photoionization cross sections vs wavelength.

(Left) Original grids, (middle) high-resolution grid, and (right) low-resolution NRLEUV grid. The high-resolution McLaughlin cross section was constructed from the cross section delivered by B. McLaughlin supplemented with Conway data below 34 Å and fit with a polynomial for a smooth transition from 56 Å to 34 Å. The data was then interpolated onto the high-resolution solar spectrum grid, which increases with a bin size of 0.01 Å. The low-resolution McLaughlin cross section was constructed from the original cross section delivered by B. McLaughlin supplemented with Conway data below 33.5 Å and fit with a polynomial for a smooth transition from 57 Å to 33.5 Å. The data was then binned into 0.5 Å bins below 100 Å and 1 Å bins above 100 Å.

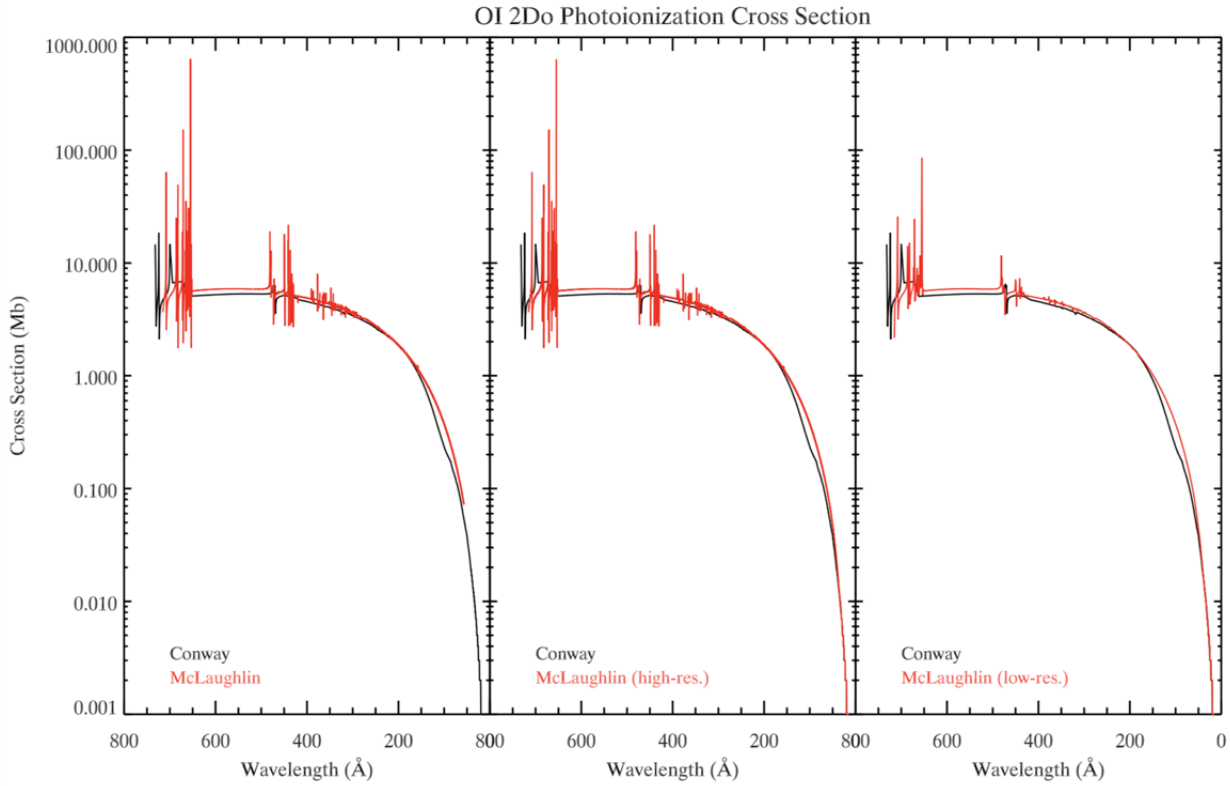

Figure 3: $O^+2s2p^3\ ^2D_0$ Photoionization cross sections vs wavelength.

(Left) Original grids, (middle) high-resolution grid, and (right) low-resolution NRLEUV grid. The high-resolution McLaughlin cross section was constructed from the cross section delivered by B. McLaughlin supplemented with Conway data below 35.5 Å and fit with a polynomial for a smooth transition from 56 Å to 35.5 Å. The data was then interpolated onto the high-resolution solar spectrum grid, which increases incrementally by 0.01 Å. The low-resolution McLaughlin cross section was constructed from the original cross section delivered by B. McLaughlin supplemented with Conway data below 38.5 Å and fit with a polynomial for a smooth transition from 57 Å to 38.5 Å. The data was then binned into 0.5 Å bins below 100 Å and 1 Å bins above 100 Å.

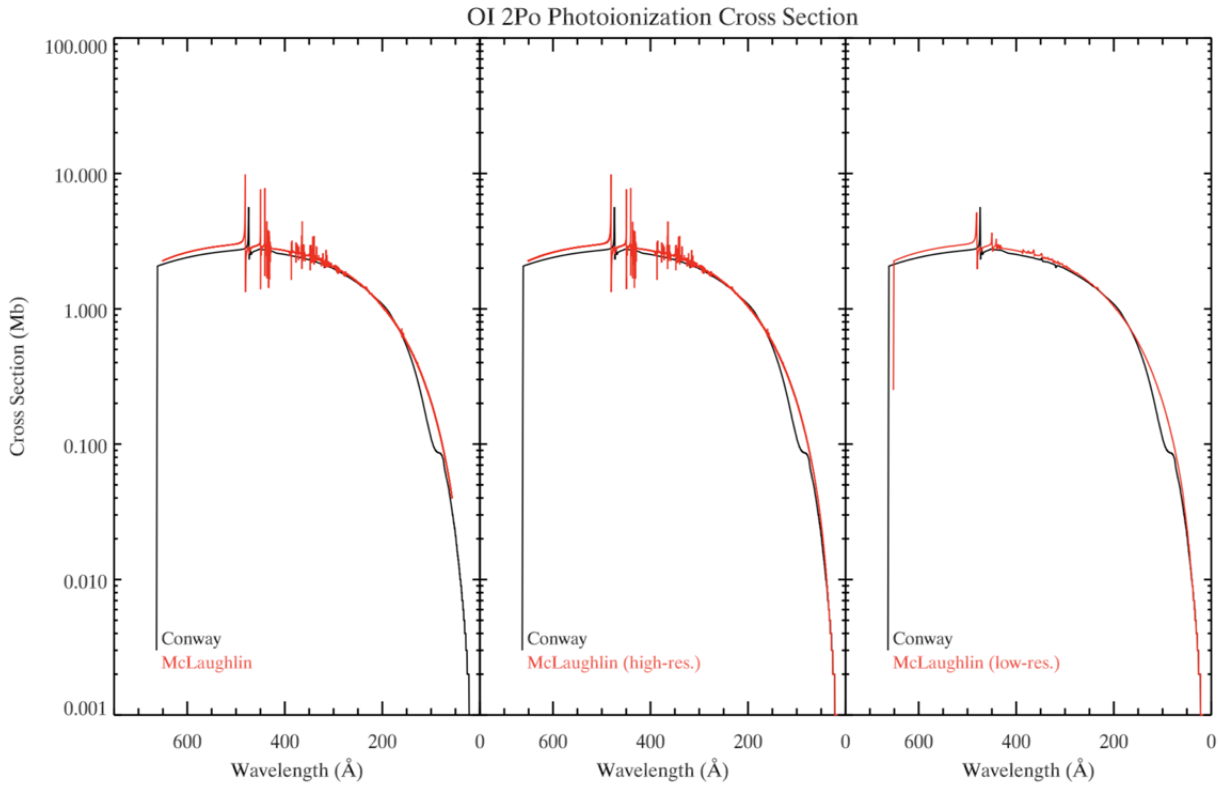

Figure 4: $O^{+}2s2p^{3}\ ^{2}P_{0}$ Photoionization cross sections vs wavelength.

(Left) Original grids, (middle) high-resolution grid, and (right) low-resolution NRLEUV grid. The high-resolution McLaughlin cross section was constructed from the cross section delivered by B. McLaughlin supplemented with Conway data below 41 Å and fit with a polynomial for a smooth transition from 56 Å to 41 Å. The data was then interpolated onto the high-resolution solar spectrum grid, which increases incrementally by 0.01 Å. The low-resolution McLaughlin cross section was constructed from the original cross section delivered by B. McLaughlin supplemented with Conway data below 41 Å and fit with a polynomial for a smooth transition from 57 Å to 41 Å. The data was then binned into 0.5 Å bins below 100 Å and 1 Å bins above 100 Å.

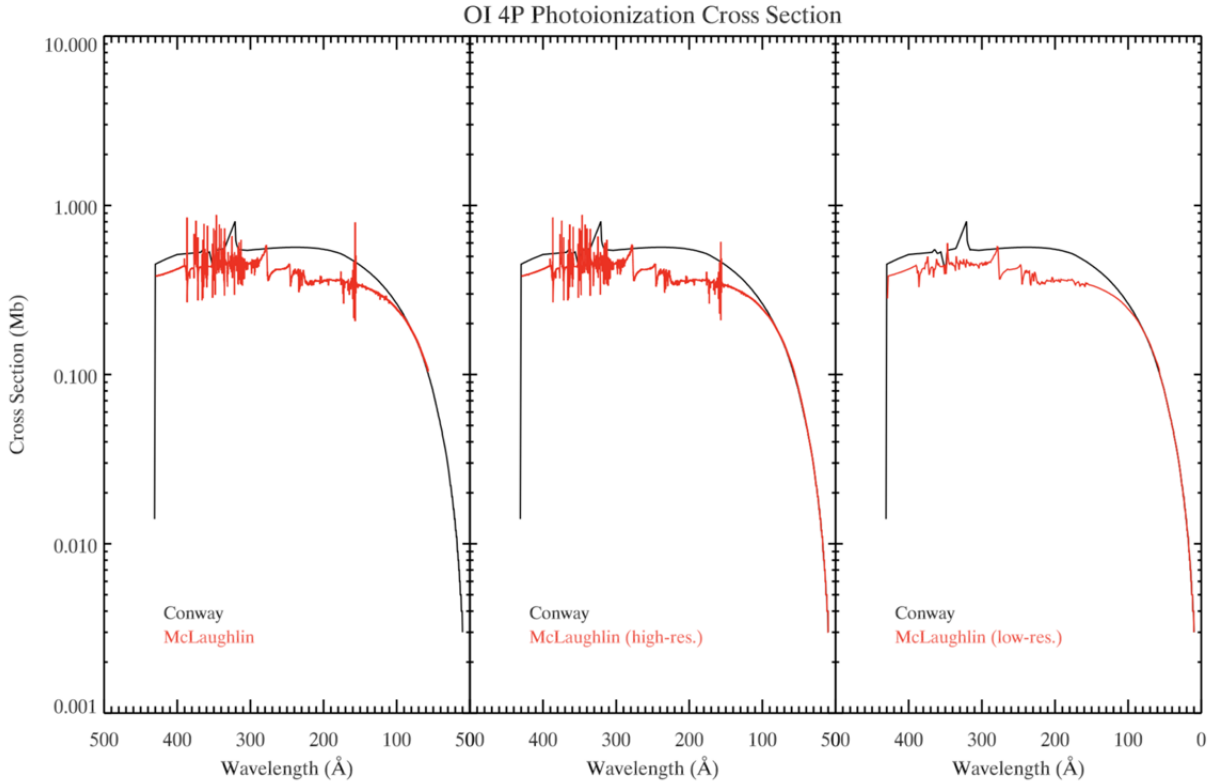

Figure 5: $O^{+}2s2p^{4}\ ^{4}P$ Photoionization cross sections vs wavelength.

(Left) Original grids, (middle) high-resolution grid, and (right) low-resolution NRLEUV grid. The high-resolution McLaughlin cross section was constructed from the cross section delivered by B. McLaughlin supplemented with Conway data below 35 Å and fit with a polynomial for a smooth transition from 56 Å to 35 Å. The data was then interpolated onto the high-resolution solar spectrum grid, which increases incrementally by 0.01 Å. The low-resolution McLaughlin cross section was constructed from the original cross section delivered by B. McLaughlin supplemented with Conway data below 57 Å. The data was then binned into 0.5 Å bins below 100 Å and 1 Å bins above 100 Å.

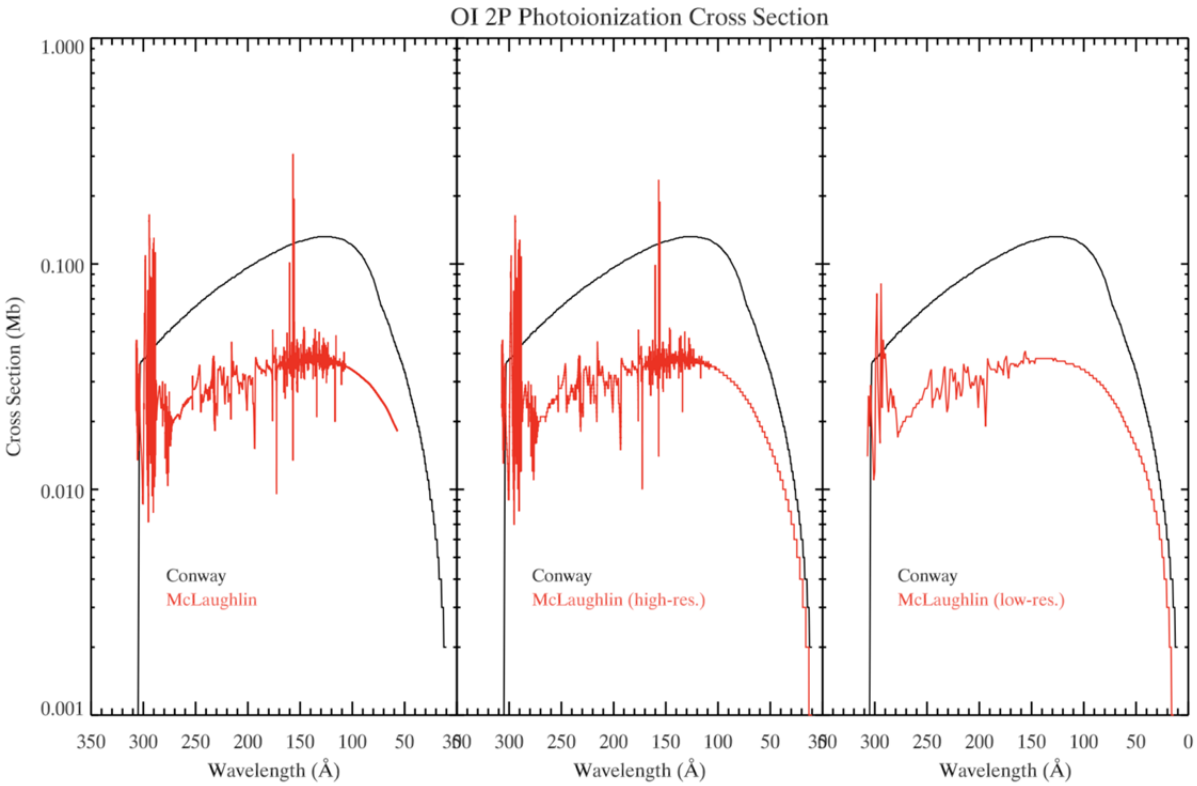

Figure 6: $O^+2s2p^4\ ^2P$ Photoionization cross sections vs wavelength.

(Left) Original grids, (middle) high-resolution grid, and (right) low-resolution NRLEUV grid. The high-resolution McLaughlin cross section was constructed from the cross section delivered by B. McLaughlin that has been fit with a polynomial to retain the expected curvature of the cross section while extending downward to lower wavelengths below 56 Å. The data was then interpolated onto the high-resolution solar spectrum grid, which increases incrementally by 0.01 Å. The low-resolution McLaughlin cross section was constructed from the original cross section delivered by B. McLaughlin supplemented with Conway data below 57 Å. The data was then binned into 0.5 Å bins below 100 Å and 1 Å bins above 100 Å.

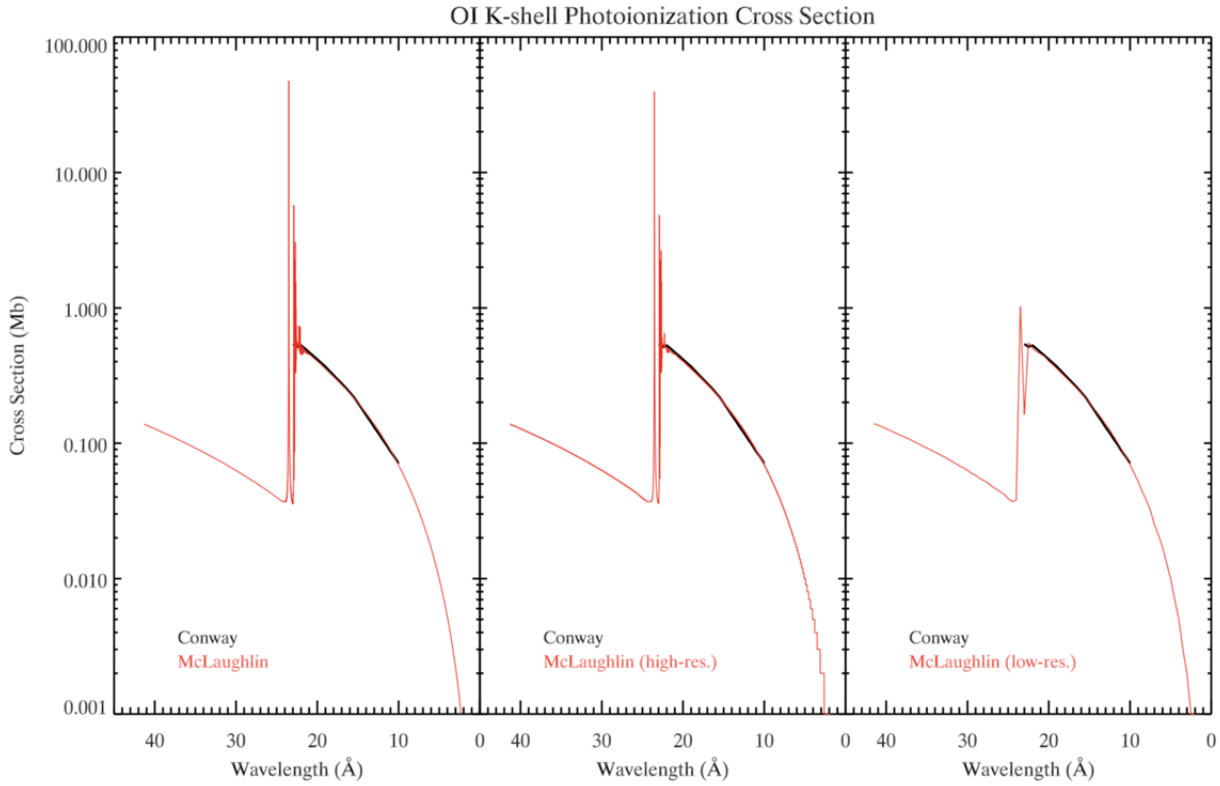

Figure 7: O^+ K-shell Photoionization cross sections vs wavelength.

(Left) Original grids, (middle) high-resolution grid, and (right) low-resolution NRLEUV grid. The high-resolution McLaughlin cross section was constructed by interpolating the k-shell cross section delivered by B. McLaughlin onto the high-resolution solar spectrum grid. The low-resolution McLaughlin cross section was constructed by binning the original cross section delivered by B. McLaughlin into 0.5 Å bins below 100 Å and 1 Å bins above 100 Å.

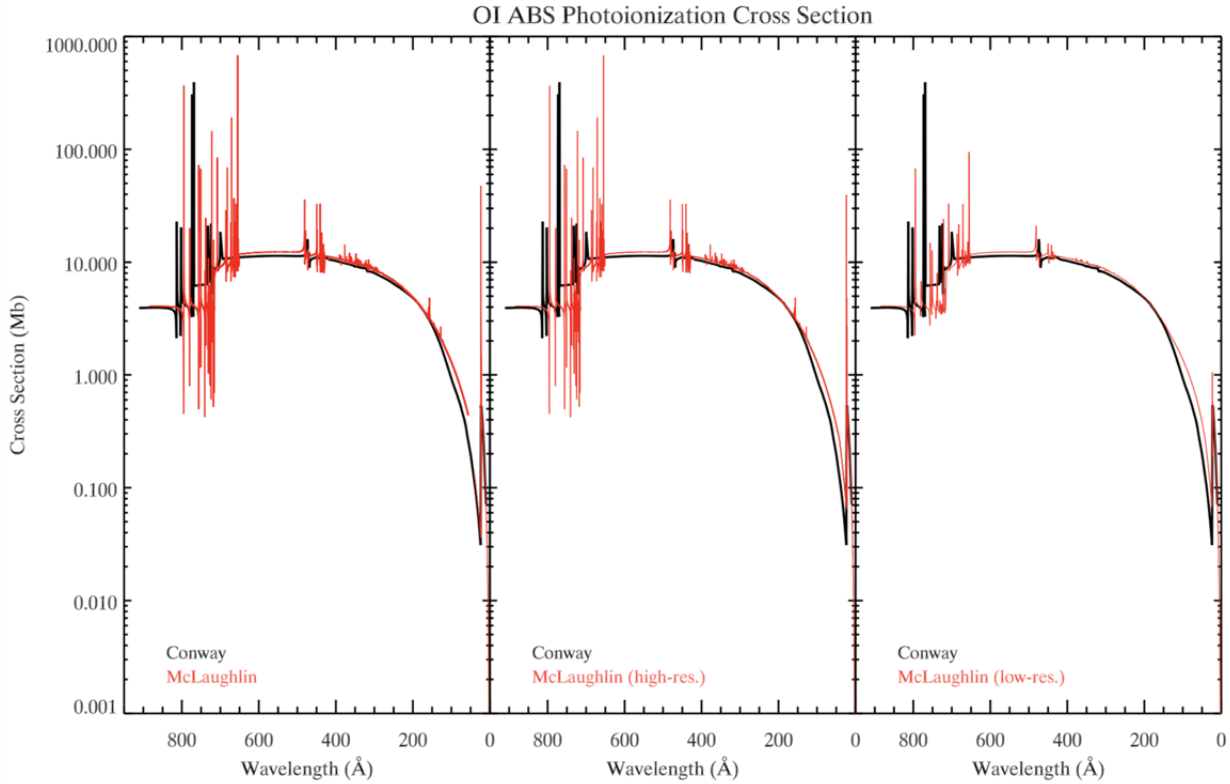

Figure 8: O^+ Absolute total photoionization cross sections vs wavelength.

(Left) Original grid, (middle) high-resolution grid, and (right) low-resolution NRLEUV grid. The high-resolution ABS McLaughlin cross section was constructed by summing the 29 partial state cross sections delivered by B. McLaughlin that are excluded in the Conway compilation and interpolating these onto the high-resolution solar spectrum grid. The high-resolution McLaughlin states are then added and the data fit with a polynomial below 57 Å to smoothly transition to lower wavelengths where the cross section is dominated by the k-shell. The low-resolution ABS McLaughlin cross section was constructed by summing the 29 partial state cross sections delivered by B. McLaughlin that are excluded in the Conway compilation and binning these onto the low-resolution NRLEUV grid with 0.5 Å bins below 100 Å and 1 Å bins above 100 Å. The low-resolution McLaughlin states are then added and the data fit with a polynomial below 57 Å to smoothly transition to lower wavelengths where the cross section is dominated by the k-shell.

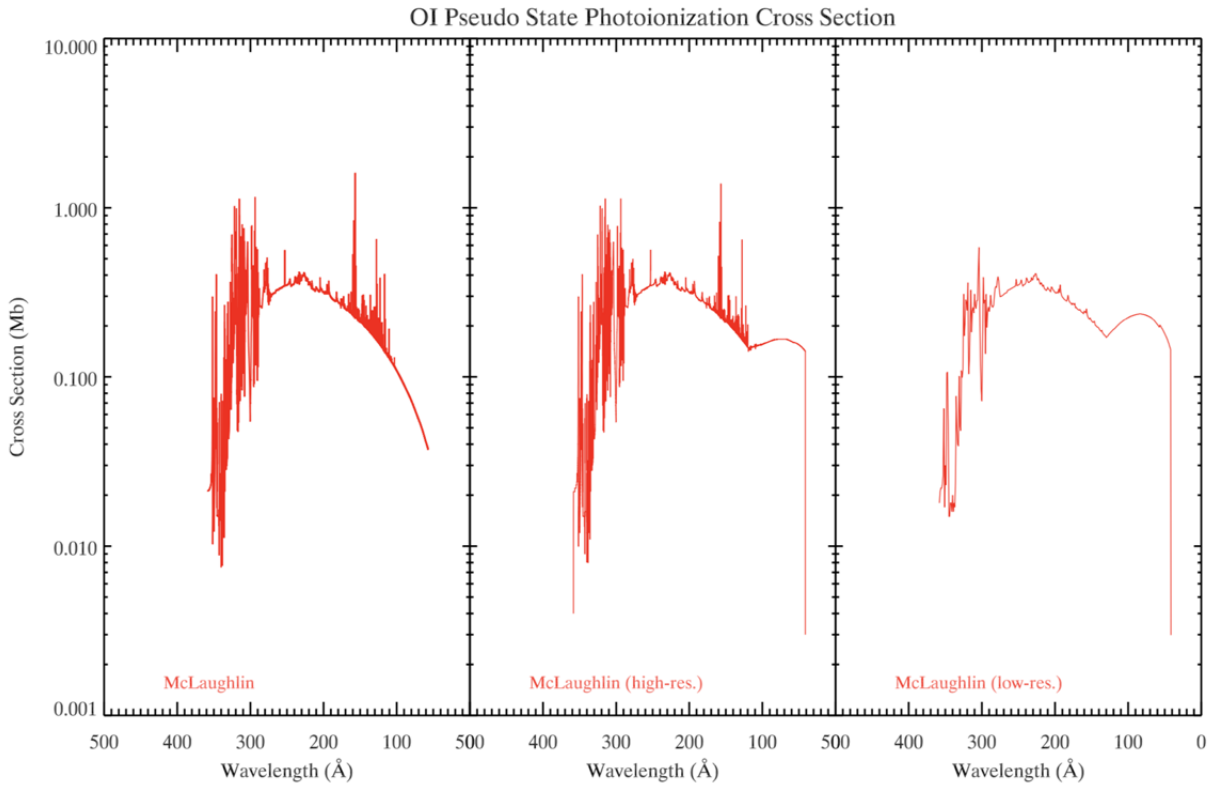

Figure 9: McLaughlin pseudo state photoionization cross sections vs wavelength.

(Left) Original grid, (middle) high-resolution grid, and (right) low-resolution NRLEUV grid. The McLaughlin pseudo state shown on the left is the sum of the remaining 29 partial states. The high-resolution pseudo state was constructed by subtracting the high-resolution partial cross sections delivered by B. McLaughlin from the high-resolution absolute total photoionization cross section. Likewise, the low-resolution pseudo state was constructed by subtracting the low-resolution partial cross sections delivered by B. McLaughlin from the low-resolution absolute total photoionization cross section.

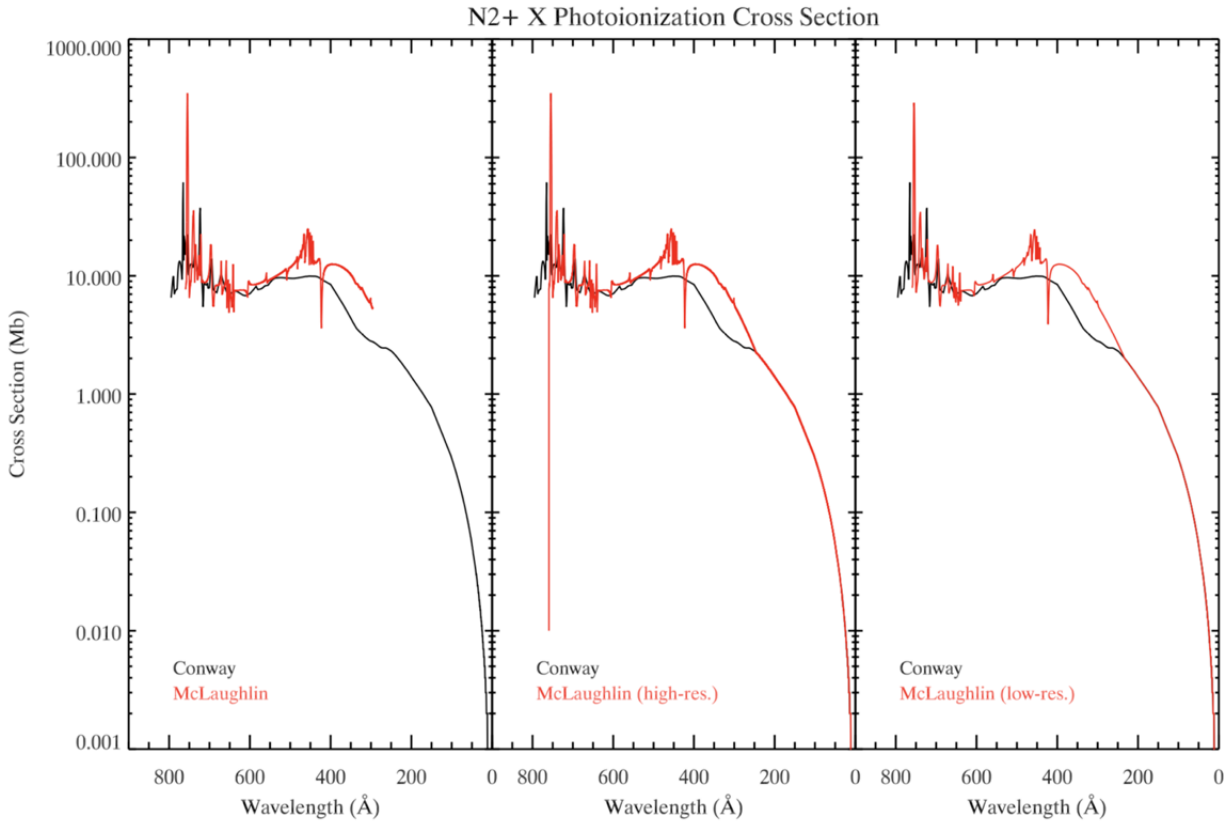

Figure 10: N_2^+ X photoionization cross sections vs wavelength.

(Left) Original grids, (middle) high-resolution grid, and (right) low-resolution NRLEUV grid. The high-resolution McLaughlin cross section was constructed from the cross section delivered by B. McLaughlin supplemented with Conway data below 295 Å and fit with a polynomial for a smooth transition from 250 Å to 295 Å. The data was then interpolated onto the high-resolution solar spectrum grid which increases incrementally by 0.01 Å. The low-resolution McLaughlin cross section was constructed from the original cross section delivered by B. McLaughlin supplemented with Conway data below 265 Å and fit with a polynomial for a smooth transition from 234 Å to 295 Å. The data was then binned into 0.5 Å bins below 100 Å and 1 Å bins above 100 Å.

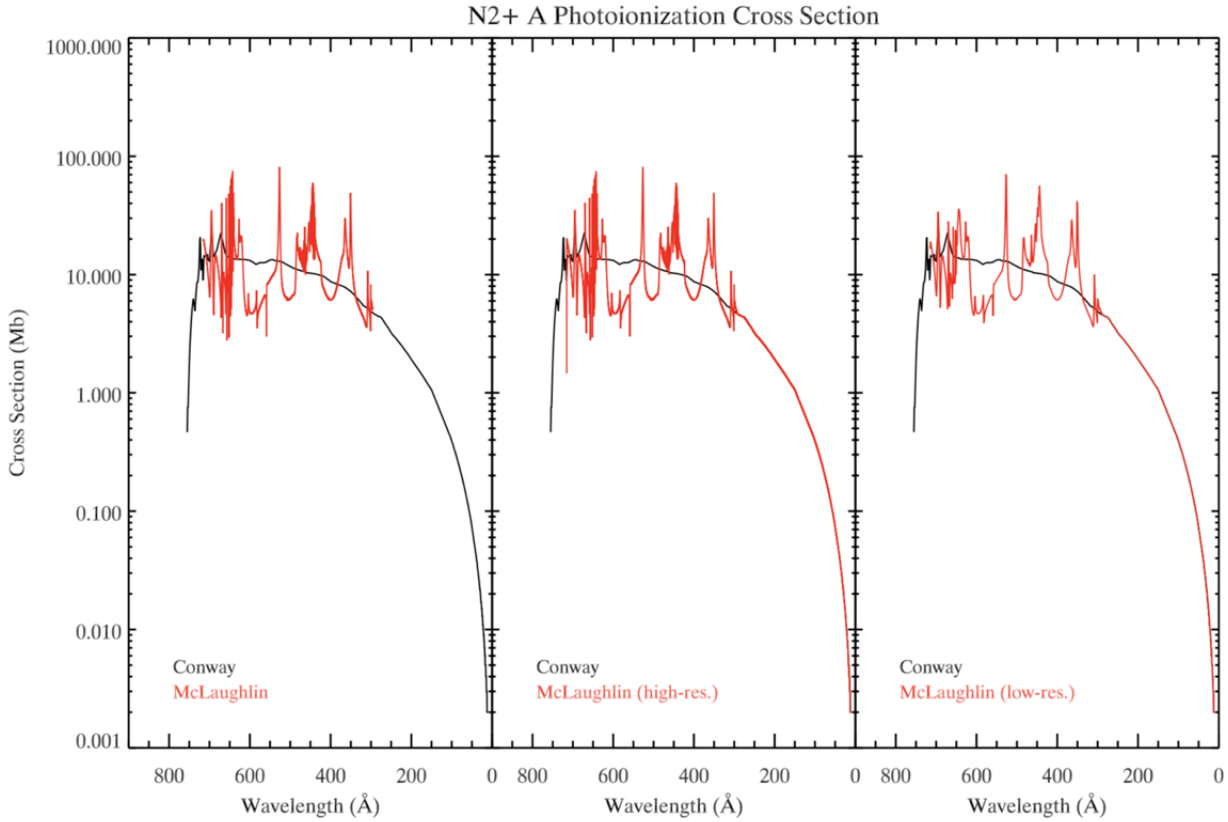

Figure 11: N_2^+ A photoionization cross sections vs wavelength.

(Left) Original grids, (middle) high-resolution grid, and (right) low-resolution NRLEUV grid. The high-resolution McLaughlin cross section was constructed from the cross section delivered by B. McLaughlin supplemented with Conway data below 295 Å and fit with a polynomial for a smooth transition from 287 Å to 295 Å. The data was then interpolated onto the high-resolution solar spectrum grid which increases incrementally by 0.01 Å. The low-resolution McLaughlin cross section was constructed from the original cross section delivered by B. McLaughlin supplemented with Conway data below 290 Å and fit with a polynomial for a smooth transition from 287 Å to 295 Å. The data was then binned into 0.5 Å bins below 100 Å and 1 Å bins above 100 Å.

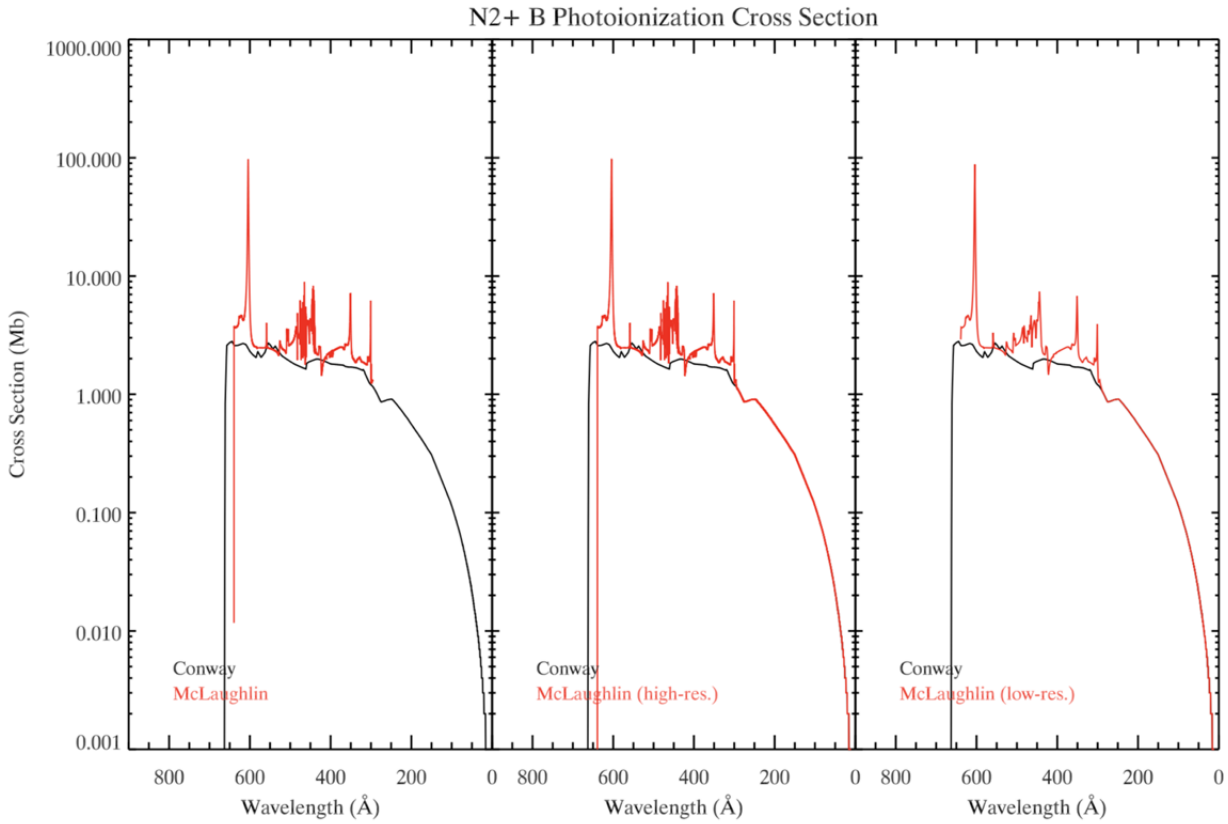

Figure 12: N_2^+ B photoionization cross sections vs wavelength.

(Left) Original grids, (middle) high-resolution grid, and (right) low-resolution NRLEUV grid. The high-resolution McLaughlin cross section was constructed from the cross section delivered by B. McLaughlin supplemented with Conway data below 295 Å and fit with a polynomial for a smooth transition from 288 Å to 295 Å. The data was then interpolated onto the high-resolution solar spectrum grid which increases incrementally by 0.01 Å. The low-resolution McLaughlin cross section was constructed from the original cross section delivered by B. McLaughlin supplemented with Conway data below 290 Å and fit with a polynomial for a smooth transition from 289 Å to 295 Å. The data was then binned into 0.5 Å bins below 100 Å and 1 Å bins above 100 Å.

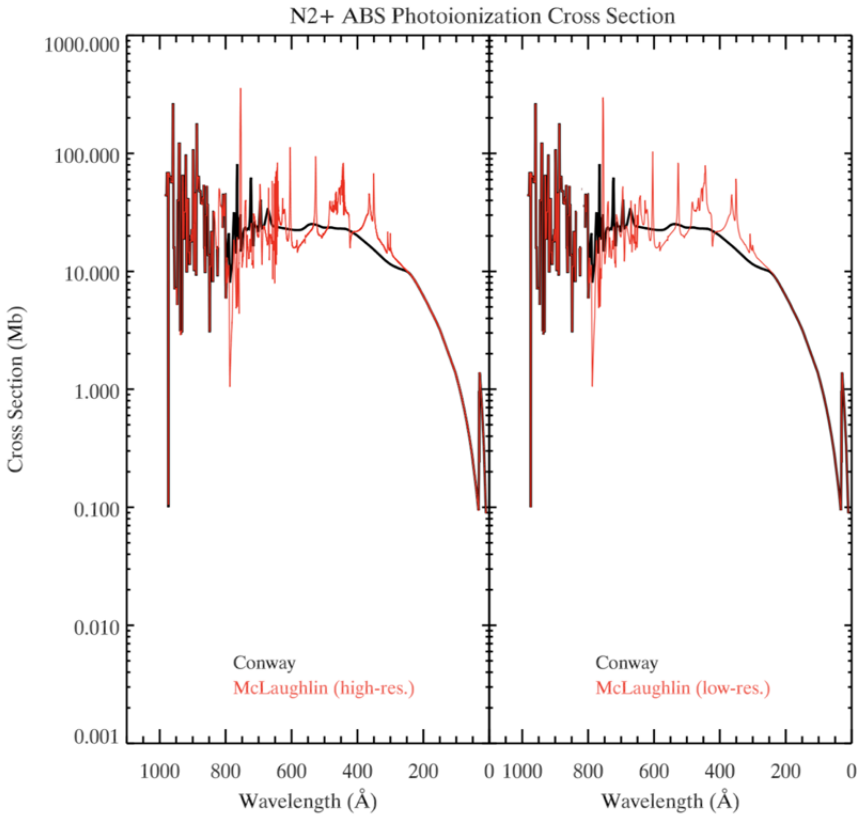

Figure 13: N_2^+ Absolute total photoionization cross sections vs wavelength.

(Left) Original grid, (middle) high-resolution grid, and (right) low-resolution NRLEUV grid. The high-resolution ABS McLaughlin cross section was constructed by interpolating the complimentary Conway compilation states onto the high-resolution solar spectrum grid and adding the high-res. McLaughlin states. The low-resolution ABS McLaughlin cross section was constructed by summing the 3 partial state cross sections delivered by B. McLaughlin and binning these onto the low-resolution NRLEUV grid with 0.5 Å bins below 100 Å and 1 Å bins above 100 Å. This was then added to the sum of the complimentary Conway compilation states on the NRLEUV grid.

KEY INSIGHTS AND RESULTS

Utilizing high-resolution O and N_2 cross sections preserve autoionization lines, previously excluded in low-resolution model inputs, that are required to properly account for electron production in the lower E-region ionosphere.

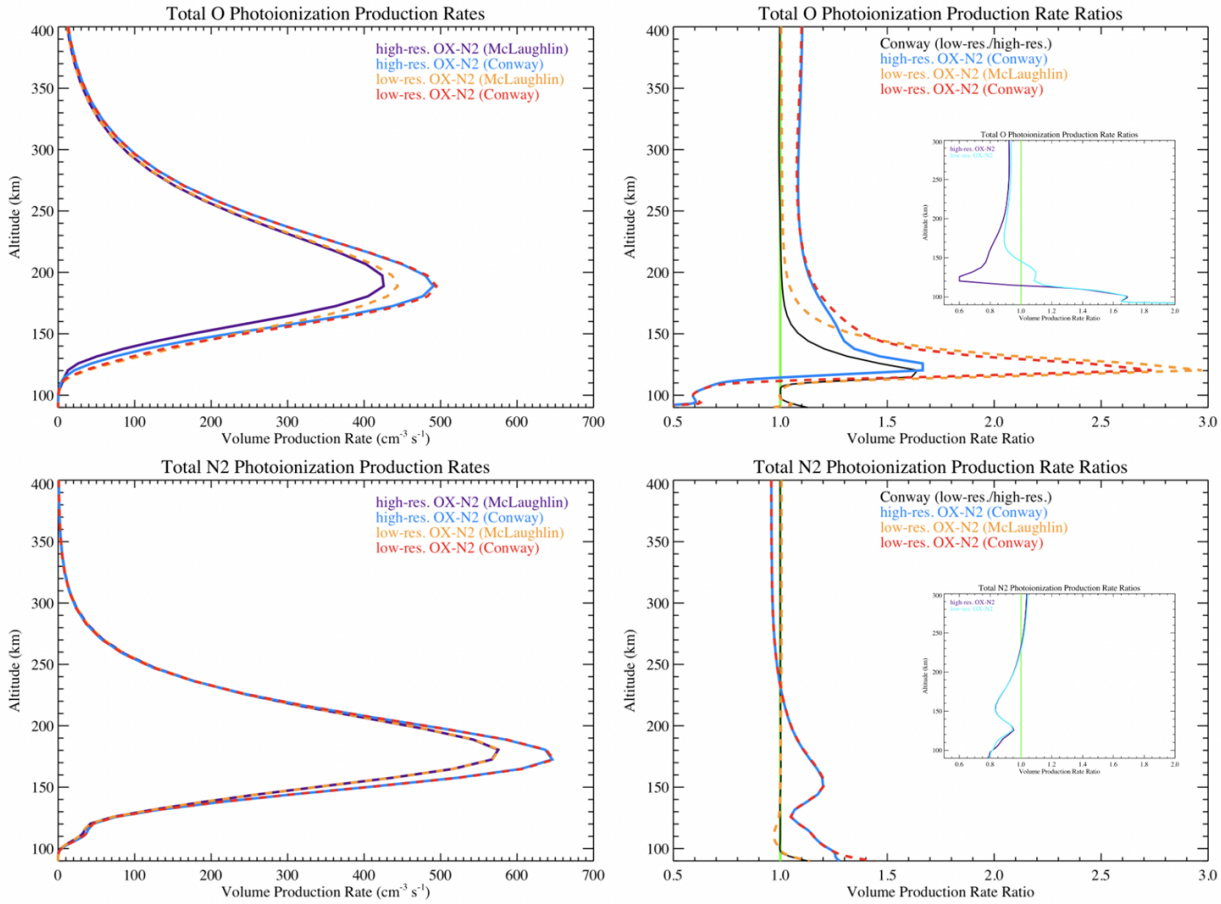

Figure 14: Total photoionization production rates and ratios (O and N_2).

(Left) Volume production rate results from AURIC with the newly incorporated high-resolution cross sections and solar irradiance spectrum for O (top) and N_2 (bottom). (Right) Volume production rate ratios for O (top) and N_2 (bottom). These are the ratios with respect to the high-resolution McLaughlin volume production rates. The ratio of low-resolution Conway and high-resolution Conway is shown in black. The insets in the ratio plots on the right show the volume production rate ratios of O and N_2 for McLaughlin/Conway cross sections of like resolution. The high-resolution case is shown in purple and the low-resolution case is shown in cyan. Unity is shown in green.

As seen in Figure 14 (left column), the volume production rates for the Conway cross sections are relatively higher for the majority of the altitude profile for both O and N_2. Below 200 km the impact of the new McLaughlin cross sections becomes more apparent in the O production rate ratios. Plots in the right column of Figure 14 show the production rate ratios with respect to the model result calculated using the high-

resolution McLaughlin cross sections. The sharp peaks in the low-resolution cross section ratios at 120 km, shown in yellow and red, indicate that low-resolution cross sections allow the production of more electrons at higher altitudes by more than a factor of 3. The effect of cross section resolution on production rates is made clearer by the black line in Figure 14, which represents the ratio of the production rates using low- to high-resolution Conway cross sections, and illustrates that the peak feature is not inherent to ratios with respect to the model results utilizing the high-resolution McLaughlin cross sections, although it is more pronounced. The smaller peak in the high-resolution Conway ratio at 125 km, shown in blue, illustrates that this effect is not entirely due to the cross section resolution but also the cross section values themselves and perhaps the solar spectral irradiance resolution. The high-resolution McLaughlin cross sections allow for deeper penetration of electrons into the atmosphere dominating effects below 115 km by upwards of 40% for the high- and low-resolution Conway cross sections. The reduced opacity of the thermosphere within the low dips in the autoionization lines of the high-resolution McLaughlin O cross sections allows photons to leak through to lower altitudes and produce greater photoionization rates. The inset plots show the McLaughlin/Conway production rate ratios for like resolutions. These ratios for O demonstrate that below 115 km it is primarily the McLaughlin cross section itself that drives the increased (70%) volume production rate. Between 115 – 200 km, cross section resolution appears to have a greater impact with a 40% drop in the production rate for high-resolution cross sections at 120 km (shown in purple) and a 10% increase in the low-resolution cross section case (shown in cyan).

The impact of the newly improved cross sections is less pronounced for the N_2 model results; however, this may be attributed to the fact that high-resolution cross sections provided by McLaughlin are only available for three states. Above 230 km, the N_2 volume production rate ratios for the Conway cross sections show a constant 5% difference indicating that the new high-resolution McLaughlin cross sections allow for greater contributions in this altitude range. Conversely, below 250 km the Conway cross sections allow for greater contribution to the N_2 production rates as illustrated by the increasing production rate ratio. The divergence from the low-resolution McLaughlin case (shown in yellow) indicates smaller resolution effects at approximately 110 km. This is further supported by the inset plot in the bottom right of Figure 14 that again shows the McLaughlin/Conway production rate ratios for like resolutions. As depicted, above 230 km the McLaughlin cross sections produce large production rates regardless of resolution; however, below 230 km the Conway cross sections produce larger rates. From 100 – 125 km, cross section resolution appears to impact the model outputs indicating an even smaller contribution from the low-resolution McLaughlin cross sections in comparison to the high-resolution cross sections.

ADDITIONAL RESULTS

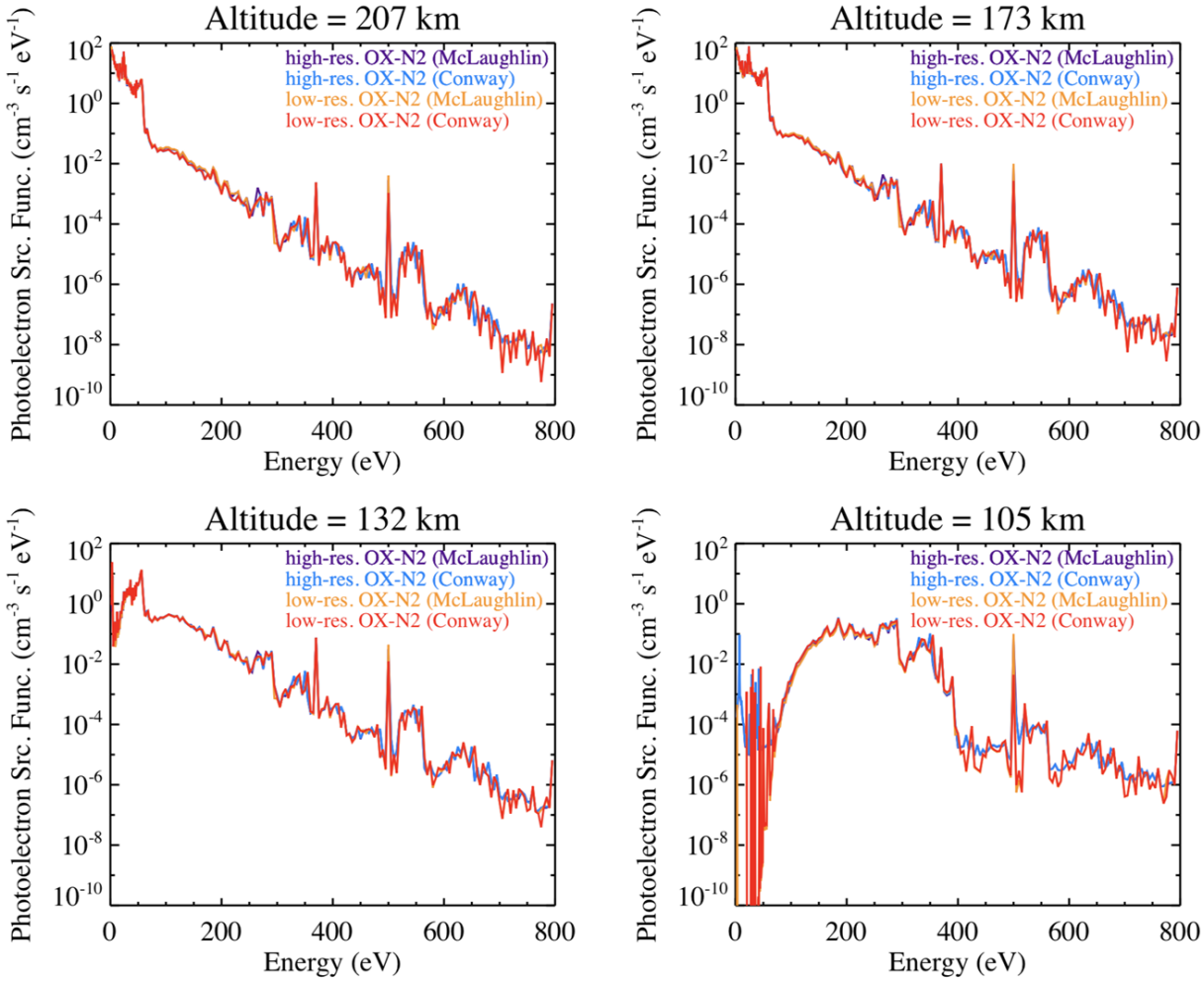

Figure 15: Photoelectron source function vs energy.

Photoelectron source functions vs energy are shown for 105, 132, 173, and 207 km utilizing high-resolution (purple) and low-resolution (yellow) McLaughlin O I cross sections and corresponding cross sections from Conway (blue and red, respectively). The computations were made using a binned NRLEUV solar irradiance spectrum for the low-resolution cross sections and 0.01 Å resolution solar spectrum for the high-resolution cross sections.

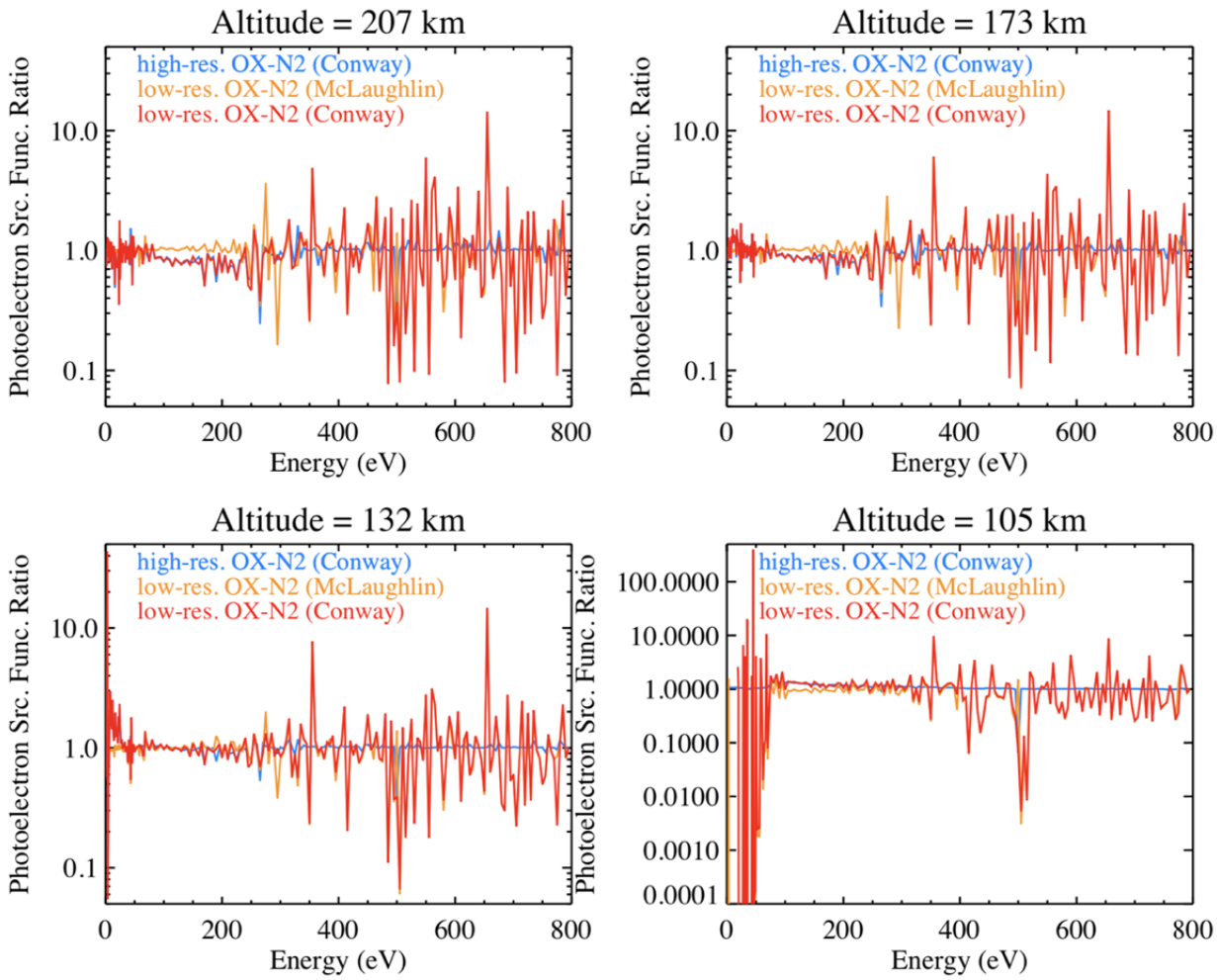

Figure 16: Photoelectron source function ratios vs energy.

Photoelectron source function ratios vs energy are shown for 105, 132, 173, and 207 km. The ratios are taken with respect to the photoelectron source function calculated using the high-resolution McLaughlin cross sections: high-resolution Conway/high-resolution McLaughlin (blue), low-resolution McLaughlin/high-resolution McLaughlin (yellow), and low-resolution Conway/high-resolution McLaughlin (red). The photoelectron source functions are in general agreement at energies less than 200 eV, but diverge at greater energies. At 500 eV the low-resolution ratios decrease by at least an order of magnitude and then increase by over an order of magnitude at 650 eV.

Figure 15 shows that the photoelectron source function typically declines as the energy increases for all cross section cases and at all altitudes, although large oscillations are observed at low energies at 105 km. Figure 16 illustrates cross section resolution impacts in the low-resolution McLaughlin and Conway ratios, which exhibit large oscillations at all altitudes. For 207, 173, and 132 km the oscillations dominate higher energy values whereas at 105 km the large oscillations occur below 100 eV. The high-resolution Conway resolution ratio (blue line) shows fewer and smaller oscillations at high energies in comparison to the low-resolution cases at all altitudes. The close to unity behavior indicates that the oscillations seen in the other cases are driven by the cross section resolution.

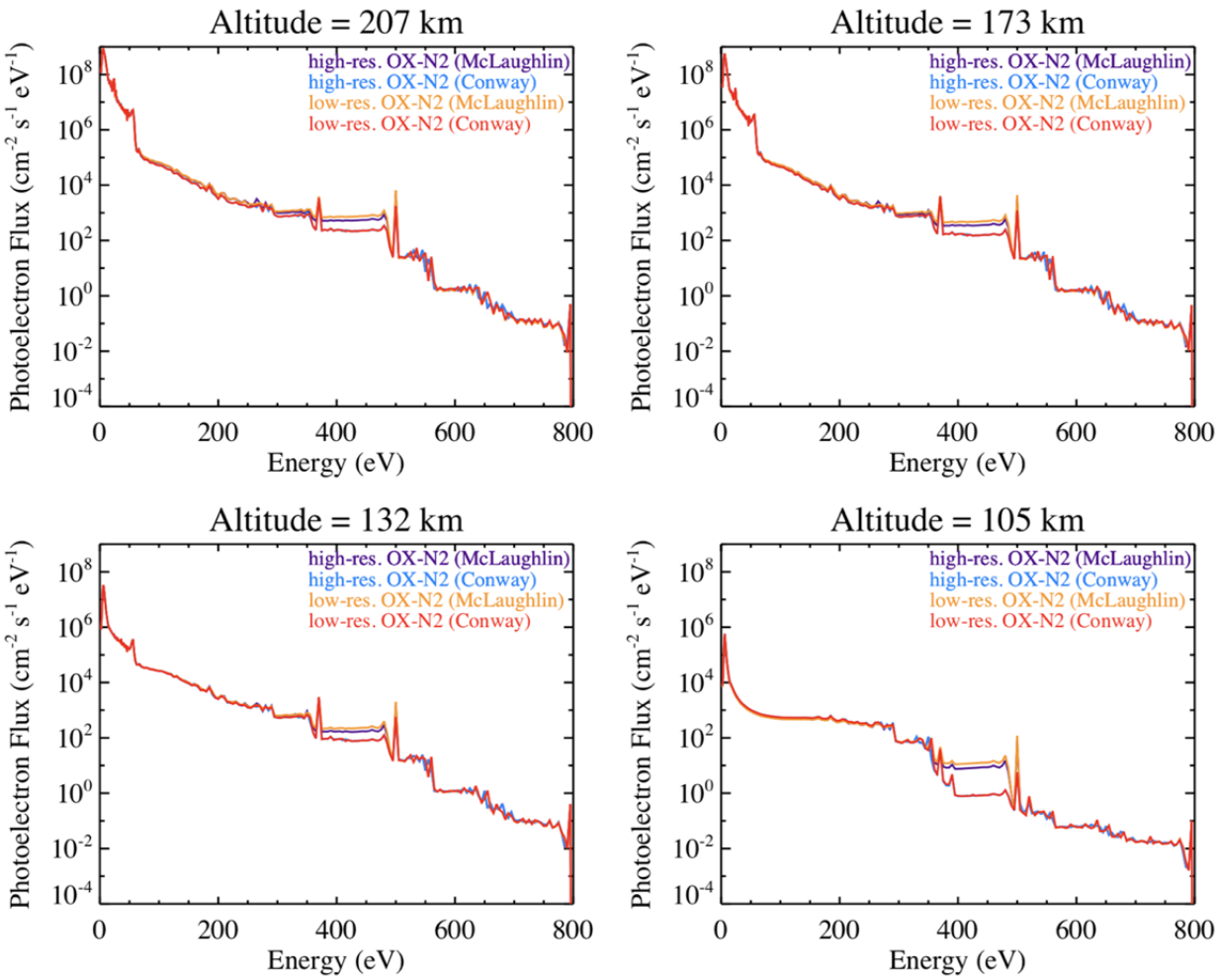

Figure 17: Photoelectron flux vs energy.

Photoelectron fluxes vs energy are shown at 105, 132, 173, and 207 km utilizing the high-resolution (purple) and low-resolution (yellow) McLaughlin cross sections and corresponding cross sections from Conway (blue and red respectively). The computations were made using a binned NRLEUV solar spectrum for the low-resolution cross sections and a 0.01 Å resolution solar spectrum for the high-resolution cross sections.

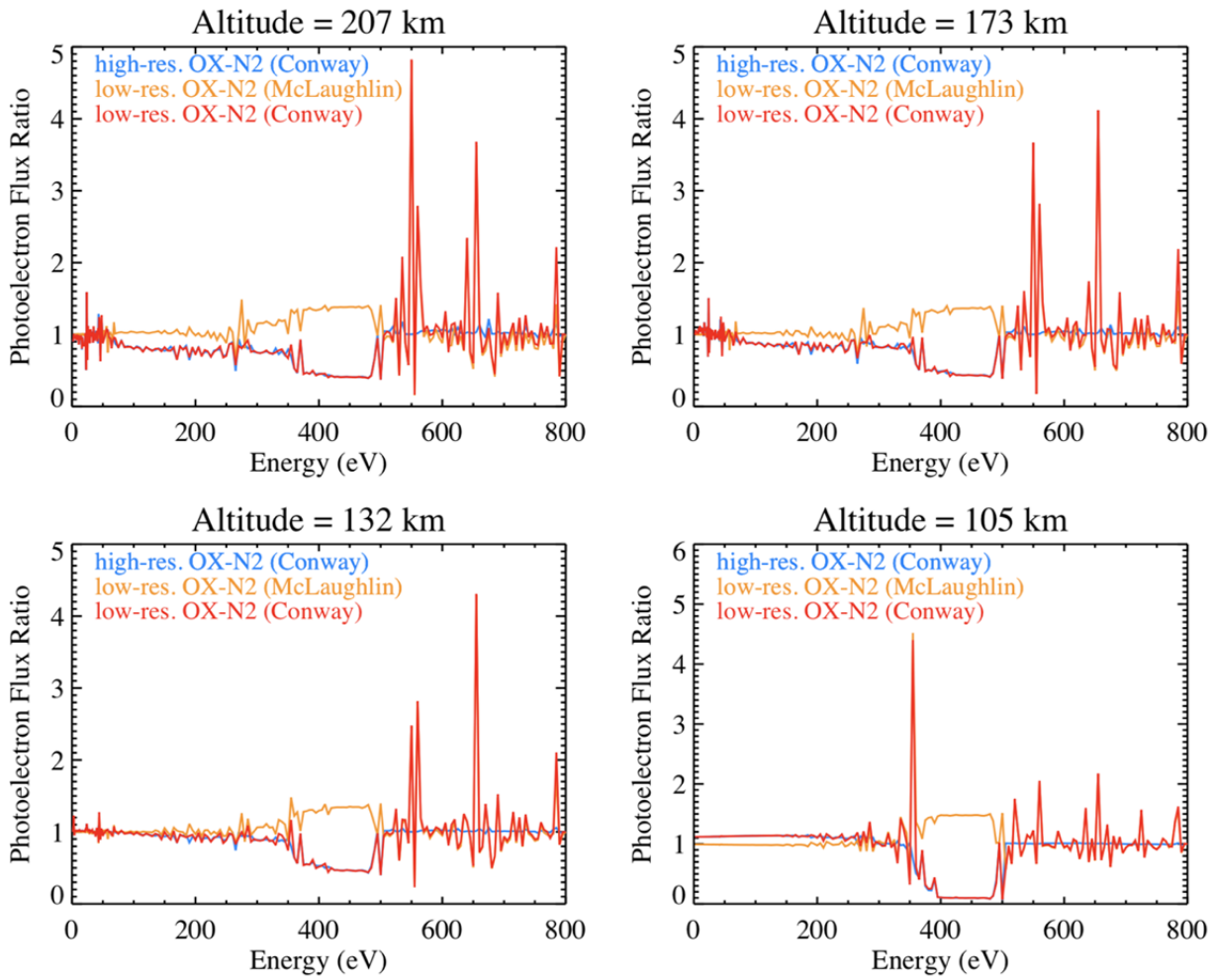

Figure 18: Photoelectron flux ratios vs energy.

Photoelectron flux ratios vs energy are shown at 105, 132, 173, and 207 km. The ratios are taken with respect to the photoelectron fluxes calculated with the high-resolution McLaughlin O I cross sections: high-resolution Conway/high-resolution McLaughlin (blue), low-resolution McLaughlin/high-resolution McLaughlin (yellow), and low-resolution Conway/high-resolution McLaughlin (red). The photoelectron flux ratios exhibit some common features with small fluctuations at ~50 eV and peaks at 550 eV, 650 eV, and ~800 eV for the low-resolution cross sections above 105 km. The ratios between 350-500 eV decrease from about 0.4 above 105 km to 0.1 at an altitude of 105 km for calculations using the Conway cross sections (blue and red) indicating larger fluxes in the high-resolution McLaughlin model runs at these energies lower in the mesosphere.

Figure 17 consistently shows a range from approximately 375 - 475 eV where the photoelectron flux from model results calculated using McLaughlin cross sections is greater than those produced utilizing the Conway compilation at all altitudes shown. The difference is more significant at lower altitudes (105 km) and is seen clearly in Figure 18, which shows the photoelectron flux ratios with respect to the model outputs using the high-resolution McLaughlin cross sections. The ratio at 105 km for the Conway cross sections is about 0.10 for the low- and high-resolution cases indicating that the McLaughlin cross section, and not the resolution, is driving these differences. At all altitudes shown, large oscillations in the ratios at high energies reflect the impact of the high-resolution McLaughlin cross sections. The high-resolution Conway ratio (shown in

blue) above 500 eV is relatively close to unity and supports the inference that the cross section resolution is the driving force behind these differences in the model outputs at high energies.

DISCUSSION AND FUTURE WORK

The total O ionization production rate at approximately 100 km when using the newly calculated high-resolution McLaughlin cross sections shows an ~40% increase over the low-resolution Conway [1988] compilation. Results show that cross section resolution impacts model predictions in the thermosphere below 200 km. The increased structure of the new McLaughlin cross sections relative to the Conway [1988] compilation propagates through to AURIC model outputs. We find that impacts of these changes are more significant in the total photoionization production rate of O than for N_2. The results for the O photoionization rates are consistent with the trends reported in Meier et al. [2007]. They found a peak in the ratio of 1.4 at approximately 110 km that decreases down to 0.95 at 100 km for the comparison of photoionization rates computed using Fennelly and Torr [1992] cross sections with respect to their 0.01 Å resolution theoretical O cross sections (Meier et al., 2007, Figure 3). Likewise, we see a peak ratio of about 2.7 at 120 km which decreases to 0.6 at 100 km for the low-resolution Conway ratio (Figure 14). The lower values for the total O high-resolution McLaughlin cross sections could explain the larger ratio for the peak seen at 120 km. The large dip in the ratio at 100 km that exists in light of the McLaughlin cross section values further substantiates the importance of high-resolution cross sections to the calculation of ionization rates in the lower E-region ionosphere. Our findings show increased total O photoionization production rates, and therefore increased electron densities, at lower altitudes with new high-resolution O and N_2 cross sections and solar spectrum. While the new N_2 cross sections did not yield higher photoionization rates at low altitudes, it is important to incorporate the high-resolution data in the 850 - 1050 Å range, which is a spectral region where photoionization of O_2 (and NO) is especially important for the E-region. Results utilizing the Conway [1988] O_2 cross sections at low-resolution show that O_2 contributions account for over 90% of the total volume production rate from 100 – 120 km. Incorporation of high-resolution cross sections for O_2, which undergoes approximately 30% photoionization from 796 – 1028 Å, would likely produce an even higher ionization rate, particularly at lower altitudes, and further decrease the gap between observed and modeled electron densities.

Future Work:

1.We will incorporate high-resolution O_2 cross sections provided by B. McLaughlin.

2.The team will compare results incorporating the high-resolution cross sections with experimental measurements, previous R-matrix calculations from Gillan et al. [1996], and values from Itikawa [2006].

3.We will also conduct a more detailed comparison of AURIC model results with those based on the approach from Meier et al. [2007].

4.The team will compare model results using high-resolution O, N_2, and O_2 cross sections and solar spectrum with observed electron densities derived from COSMIC data (Lei et al., 2007). AURIC model results will be compared to GLOW model results from McGranaghan et al. [2015], updated COSMIC density profiles from Pedatella et al. [2015], and Arecibo data analyzed by Sojka et al. [2014].

ABSTRACT

Accurate photoionization rates are vital for the study and understanding of planetary ionospheres. Previous model calculations of terrestrial photoionization rates lack sufficient spectral resolution to account for highly structured photoionization cross sections as well as the solar spectral irradiance. We present new photoionization rate calculations from CPI's Atmospheric Ultraviolet Radiance Integrated Code [AURIC; Strickland et al., 1999] using high-resolution (0.01 Å) solar spectra and high-resolution (0.01 Å) atomic oxygen (O) and molecular nitrogen (N_2) photoionization cross sections. Theoretical photoionization cross sections of O are determined utilizing the R-matrix plus pseudo-states (RMPS) approximation whereas N_2 cross sections are determined using the R-matrix approximation. We include 34 high-resolution partial O state photoionization cross sections and 3 high-resolution partial N_2 state photoionization cross sections with supplemental Conway [1988] tabulations for molecular oxygen and the remaining N_2 states. We find that photoionization rates computed at 0.01 Å resolution differ substantially from rates computed using low-resolution cross sections, especially in the lower thermosphere below 200 km. Specifically, we find that ionization production rate ratios exhibit variations in altitude of more than ±40% between the high- and low-resolution cases. Past low-resolution calculations at various low spectral resolutions do not sufficiently account for or preserve the highly structured auto-ionization lines in the photoionization cross sections [Meier et al., 2007]. These features, in combination with high-resolution solar spectra, allow photons to penetrate deeper into the Earth's atmosphere producing larger total ionization rates. These higher ionization rates may finally resolve data-model discrepancies in altitude profiles of electron densities due to the use of low-resolution photoionization cross sections in current E-region models.

REFERENCES

1. Abdel-Naby, S. A., C. P. Ballance, T. G. Lee, S. D. Loch, and M. S. Pindzola (2013), Electron- impact ionization of the C atom, Physical Review A, 87(2), 022,708.
2. Conway, R. R., R. R. Meier, and R. E. Huffman (1988), Satellite observations of the O I 1304, 1356 and 1641 A dayglow and the abundance of atomic oxygen in the thermosphere, Planetary and Space Science, 36, 963–973, doi:10.1016/0032-0633(88)90034-7.
3. Gillan, C. J., J. Tennyson, B. M. McLaughlin, and P. G. Burke (1996), Low-energy electron impact excitation of the nitrogen molecule: optically forbidden transitions, Journal of Physics B Atomic Molecular and Optical Physics, 29, 1531–1547, doi:10.1088/0953-4075/29/8/017.
4. Itikawa, Y. (2006), Cross Sections for Electron Collisions with Nitrogen Molecules, Journal of Physical and Chemical Reference Data, 35, 31–53, doi:10.1063/1.1937426.
5. Lei, J., S. Syndergaard, A. G. Burns, S. C. Solomon, W. Wang, Z. Zeng, R. G. Roble, Q. Wu, Y.-H. Kuo, J. M. Holt, S.-R. Zhang, D. L. Hysell, F. S. Rodrigues, and C. H. Lin (2007), Comparison of COSMIC ionospheric measurements with ground-based observations and model predictions: Preliminary results, Journal of Geophysical Research (Space Physics), 112, A07308, doi:10. 1029/2006JA012240.
6. McGranaghan, R., D. J. Knipp, S. C. Solomon, and X. Fang (2015), A fast, parameterized model of upper atmospheric ionization rates, chemistry, and conductivity, Journal of Geophysical Re- search (Space Physics), 120, 4936–4949, doi:10.1002/2015JA021146.
7. McLaughlin, B. M., T. G. Lee, J. A. Ludlow, E. Landi, S. D. Loch, M. S. Pindzola, and C. P. Ballance (2011), A large-scale R-matrix calculation for electron-impact excitation of the Ne2+, O-like ion, Journal of Physics B: Atomic, Molecular and Optical Physics, 44(17), 175,206.
8. McLaughlin, B.M., C.P. Ballance, K.P. Bowen, D.J. Gardenghi, and W.C. Stolte (2013), High Precision K-shell Photoabsorption Cross Sections for Atomic Oxygen: Experiment and Theory, Astrophysical Journal Letters, 771(1), 8, doi:10.1088/2041-8205/771/1/L8
9. Meier, R. R., B. M. McLaughlin, H. P. Warren, and J. Bishop (2007), Atomic oxygen photoioniza- tion rates computed with high resolution cross sections and solar fluxes, Geophysical Research Letters, 34, 1104, doi:10.1029/2006GL028484.
10. Pedatella, N. M., X. Yue, and W. S. Schreiner (2015), An improved inversion for formosat- 3/cosmic ionosphere electron density profiles, Journal of Geophysical Research: Space Physics, pp. n/a–n/a, doi:10.1002/2015JA021704, 2015JA021704.
11. Scully,S.W.J.,I.A´lvarez,C.Cisneros,E.D.Emmons,M.F.Gharaibeh,D.Leitner,M.S.Lubell, A. Mu¨ller, R. A. Phaneuf, R. Pu¨ttner, et al. (2006), Doubly excited resonances in the photoion- ization spectrum of Li+: experiment and theory, Journal of Physics B: Atomic, Molecular and Optical Physics, 39(18), 3957.
12. Sojka, J. J., J. B. Jensen, M. David, R. W. Schunk, T. Woods, F. Eparvier, M. P. Sulzer, S. A. Gon- zalez, and J. V. Eccles (2014), Ionospheric model-observation comparisons: E layer at arecibo incorporation of sdo-eve solar irradiances, Journal of Geophysical Research: Space Physics, 119(5), 3844–3856, doi:10.1002/2013JA019528, 2013JA019528.
13. Strickland, D. J., J. Bishop, J. S. Evans, T. Majeed, P. M. Shen, R. J. Cox, R. Link, and R. E. Huff- man (1999), Atmospheric ultraviolet radiance integrated code (AURIC): theory, software archi- tecture, inputs, and selected results., Journal of Quantatitive Spectroscopy and Radiative Trans- fer, 62, 689–742, doi:10.1016/S0022-4073(98)00098-3.
14. Tayal, S.S. and Zatsarinny, O. (2016), B -spline R -matrix-with-pseudostates approach for excitation and ionization of atomic oxygen by electron collisions, Physics Review A, 94(4), doi:10.1103/PhysRevA.94.042707